frontiers in Earth Science

TYPE Original Research
PUBLISHED 24 August 2026
DOI 10.3389/feart.2026.1869925

Snow melting phases detection using apparent thermal inertia, radar data and numerical modelling

Olga Gatti[1], Biagio Di Mauro[2]*, Carlo Marin[3], Roberto Garzonio[1], Gabriele Bramati[4], Valentina Premier[3], Claudia Notarnicola[3], Simone Pettinato[5], Claudia Ravasio[1], Edoardo Cremonese[6], Paolo Pogliotti[7] and Roberto Colombo[1]

[1]Department of Earth and Environmental Sciences, University of Milano-Bicocca, Milan, Italy, [2]Institute of Polar Sciences – National Research Council of Italy, ISP – CNR, Milan, Italy, [3]EURAC Research – Institute for Earth Observation, Bolzano, Italy, [4]Remote Sensing Laboratories, Department of Geography, University of Zurich, Zurich, Switzerland, [5]Institute of Applied Physics, IFAC – National Research Council, IFAC-CNR, Firenze, Italy, [6]CIMA Research Foundation, Savona, Italy, [7]Climate Change Unit, Environmental Protection Agency of Aosta Valley, Aosta, Italy

OPEN ACCESS

EDITED BY
Markus Michael Frey,
British Antarctic Survey (BAS),
United Kingdom

REVIEWED BY
Paolo Perret,
Fondazione Montagna Sicura, Italy
Sara Darychuk,
University of Northern British
Columbia, Canada

*CORRESPONDENCE
Biagio Di Mauro,
biagio.dimauro@cnr.it

RECEIVED 30 April 2026
REVISED 25 July 2026
ACCEPTED 28 July 2026
PUBLISHED 24 August 2026

CITATION
Gatti O, Di Mauro B, Marin C, Garzonio R, Bramati G, Premier V, Notarnicola C, Pettinato S, Ravasio C, Cremonese E, Pogliotti P and Colombo R (2026) Snow melting phases detection using apparent thermal inertia, radar data and numerical modelling.
Front. Earth Sci. 14:1869925.
doi: 10.3389/feart.2026.1869925

The timing of snowmelt has a crucial relevance for water management in mountain areas. Several approaches have been developed to detect the state of snow during the melting season using satellite observations, ground data, and numerical modelling, but these have rarely been compared directly. In this study, we used multitemporal (2016–2021) data from two meteorological stations located in the Aosta Valley (Western European Alps, Italy), namely, Torgnon (2050 m asl–sub-Alpine site) and Cime Bianche (3100 m asl–Alpine site), to force the SNOWPACK model and analyse the seasonal evolution of snow. Furthermore, we combined optical and thermal data continuously measured at the two sites to calculate the Apparent thermal inertia of snow (APs). This variable was found to resemble snow melting phases, i.e., warming, ripening, and output. In addition, Sentinel-1 Synthetic Aperture Radar (SAR) backscattering time series were analysed for both sites and compared with COSMO SkyMed backscattering time series. We extracted the start, end, and duration of the snow phases from all three datasets (APs, Sentinel-1, and SNOWPACK simulations) and compared them to assess their consistency. The comparison between Sentinel-1 and COSMO SkyMed demonstrates that both sensors independently capture the main stages of the snowmelt process showing consistent seasonal backscatter dynamics. While aggregated results showed a consistent representation of snowmelt among the three approaches ($0.86 < R^2 < 0.91$; $4 < RMSE<12$), a phase- and site-specific analysis revealed that the Warming phase yielded lower statistics with respect to the Ripening and Output phase. and the comparison of warming-phase detection confirms an earlier onset of melting at the sub-Alpine site (DOY 60–160) than Alpine site (DOY 100–200), while also revealing method-dependent differences in phase identification. The estimated timing uncertainties correspond to 2.9%–8.9% of the snow season. Thus, these phase onset estimates are currently better suited to model evaluation and data assimilation than standalone peak-runoff prediction, and this uncertainty should be explicitly propagated in operational forecasting.

KEYWORDS

albedo, cryosphere hydrological processes, modeling, remote sensing, snowmelt dynamics, snowpack, surface temperature

1 Introduction

The timing of snowmelt is crucial for water management in mountain regions. Snowmelt rates can be intensified by increasing air temperature (Semmens et al., 2013), rain-on-snow events (Wever et al., 2014), light-absorbing impurities deposition or resurfacing (Di Mauro et al., 2019; Dumont et al., 2020) or it can be dampened by the occurrence of snowfalls in late season and refreeze events (Yue et al., 2022). These interacting processes make it difficult to determine the onset of snowmelt in mountain areas and polar regions.

Understanding the different phases of snow accumulation and melting is essential for grasping the hydrological dynamics of alpine catchments. Snow acts as a crucial water reservoir, feeding rivers and lakes during spring and summer. The timing and intensity of snowmelt directly affect water availability, flood (Thirel et al., 2013), drought risk, and hydroelectric production (Magnusson et al., 2020). Moreover, the interannual variability of snow accumulation is closely linked to climate change, making continuous monitoring vital. Accurately identifying snowmelt phases helps improve hydrological models, optimize agricultural planning (Qin et al., 2020), and support hydroelectric energy production (Magnusson et al., 2020). In Alpine regions, where topography and weather conditions are complex, this knowledge becomes even more strategic for sustainable land management.

Several attempts have been made to detect the surficial state of snow during the melting season by using both satellite observations, ground data, and numerical modelling. Main effort has been made by exploiting SAR data (Carletti et al., 2025; Lund et al., 2022; Marin et al., 2020; Pettinato et al., 2022; Darychuk et al., 2025), passive microwave observations (Picard and Fily, 2006), and apparent thermal inertia (Colombo et al., 2019). While SAR and passive microwave observations are well-established methods for snow melt detection, more recently optical and thermal data have been exploited for determining the melting phases of snow (Colombo et al., 2019; 2023). This latter method combines snow surface broadband albedo (hereafter referred to as albedo) and surface temperature to determine the APs of snow, that has been observed to track snow melting in space and time.

In the context of the snow melting process, three main phases have been ideally identified by scientists with the aim of studying in detail the evolution of the snowpack (Dingman, 2015): warming phase, ripening (or moistening) phase, and the output (or runoff) phase (Colombo et al., 2019; Marin et al., 2020). During the warming phase, the solar radiation intensifies causing the increase in the air temperature and, consequently, the average snowpack temperature starts to increase until it reaches 0 °C. From this moment onwards and for the following phases the snowpack will be isothermal. After this initial phase, snow starts to melt and the liquid water fills the pores between grains without being released. At the end of this phase the snowpack is ripe and cannot retain any more liquid water, the maximum retention capacity of the pores is exceeded and the output phase occurs. In fact, further inputs of energy accelerate the melting process and increase the production of liquid water that is released as output. This phase is marked by the presence of runoff until the snowpack has completely melted out.

Although various temporal datasets have been used to identify snowmelt phases, no study has yet compared phases estimates derived from different sources. This represents the innovative contribution of our study and highlights the potential for synergies between current and future satellite missions for the study of the cryosphere. In this context, we present a three-way comparison of snow melting phases detection using Apparent Thermal Inertia, radar backscattering data, and numerical modelling, applied to Alpine and sub-Alpine sites located in the Aosta Valley (Italy, Pennine Alps).

In addition to these approaches, this study presents a comparison between C- and X-band radar backscattering time series to evaluate their capability to independently capture the evolution of the snowmelt process. Radar backscatter observations acquired at different microwave frequencies provide valuable insights into the physical mechanisms that govern snowmelt. Both the Sentinel-1 (C-band, 5.405 GHz) and COSMO-SkyMed (X-band, 9.6 GHz) missions offer dense temporal coverage over Alpine regions, enabling a detailed analysis of the temporal evolution of the radar signal during the melting period. Although the two frequencies differ in penetration depth and sensitivity to liquid water content, their temporal behaviour has never been directly compared for snowmelt detection.

2 Data and methods

2.1 Study area

This study focuses on two experimental sites (Figure 1A) in the Aosta Valley (Pennine Alps, Valtournenche, Italy), where multi-source snow monitoring has been carried out over five hydrological seasons (2016–2021). The two sites, namely, Cime Bianche (Figure 1B) and Torgnon (Figure 1C), differ in elevation and climatic conditions, providing complementary environments for investigating snowpack evolution.

Cime Bianche (45.920°N, 7.694°E, 3,100 m a.s.l.) is located at the head of the Valtournenche valley on the Italian side of the Matterhorn. The site lies on a small west-facing plateau characterized by uneven topography and depressions that strongly influence the spatial variability of snow cover (Pogliotti et al., 2015). Snow typically persists from October

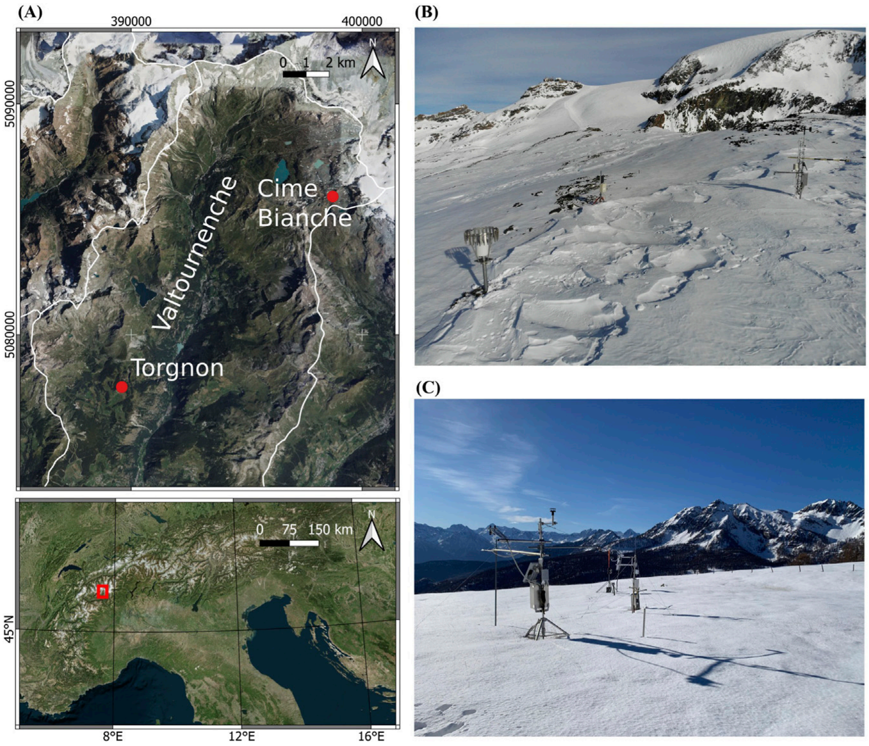

FIGURE 1
(A) Geographical location of the Cime Bianche and Torgnon field sites in the Aosta Valley, Northern Italy. **(B)** Photographs of the experimental sites at Cime Bianche (3,100 m a.s.l.) **(B)** and Torgnon (2050 m a.s.l.) **(C)**.

through June. Frequent NE–NW winds enhance redistribution processes, contributing to pronounced heterogeneity in snow depth. The site has been monitored since 2005, initially for permafrost studies (Pogliotti et al., 2015) and is equipped with an automatic weather station (AWS) that records standard meteorological variables (air temperature, surface temperature, relative humidity, atmospheric pressure, wind speed and direction, incoming and outgoing short- and long-wave solar radiation) and snow depth at 10-min resolution. Precipitation data (solid and liquid) have been collected since 2009, while snow water equivalent (SWE) is not measured at this location.

Torgnon (45.844°N, 7.578°E, 2050 m a.s.l.) is situated in a flat grassland area at subalpine elevation. The site experiences a semi-continental climate and is typically snow-covered from late October to late May (Colombo et al., 2019). An AWS installed in 2009 provides continuous meteorological and snow-related observations, including air temperature, surficial temperature, snow depth, SWE, albedo, precipitation, and wind.

Together, these sites provide contrasting high-alpine and subalpine conditions that allow for comparative analysis of melt dynamics. This contrast is clearly reflected in the mean snow-depth evolution over the five study winters (Figure 2): Cime Bianche consistently develops a deeper and more variable snowpack, largely influenced by wind redistribution from January to April, whereas Torgnon shows a more uniform and shallower accumulation typical of subalpine environments.

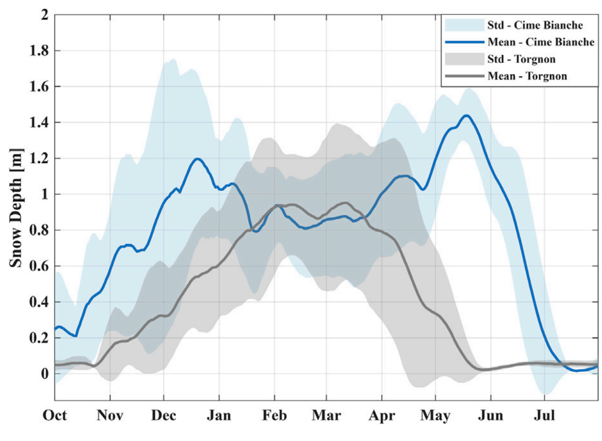

FIGURE 2
Mean seasonal snow depth and associated standard deviation at Cime Bianche and Torgnon over the five study winters (2016–2021). The high-alpine site of Cime Bianche shows consistently deeper snowpacks and marked variability due to wind redistribution, while Torgnon displays a more stable subalpine accumulation pattern.

2.2 Estimation of snow thermal inertia

Thermal inertia is a physical property of surface materials that governs their resistance to temperature variations under both diurnal and seasonal heating (Nearing et al., 2012).

APs, derived from remote sensing, has been shown to closely approximate physically measured thermal inertia, as demonstrated in numerous studies (Ma et al., 2013; Minacapilli et al., 2009; Short and Stuart, 1982; Tian et al., 2015; Van doninck et al., 2011; Wang et al., 2010). A key advantage of APs is that it can be estimated directly from remote sensing observations, allowing analyses to be conducted efficiently over large areas (e.g., entire catchments). In this study, we adopted the formulation (1) proposed by Xue and Cracknell (1995) and further developed by Maltese et al. (2013), which has also been successfully applied to snow surface (Colombo et al., 2019; 2023).

$$APs = \frac{(1-a)SW_{in}}{\Delta T_{(t_2-t_1)}} \frac{A_1 \cos(\omega t_1-\delta_1)-\cos(\omega t_2-\delta_1)}{\sqrt{\omega}\sqrt{1+\frac{1}{b}+\frac{1}{2b^2}}} \left[Jm^{-2}K^{-1}s^{-\frac{1}{2}}\right] \quad (1)$$

The method combines snow shortwave co-albedo (1-α) with the difference in snow temperature (ΔT) between night and day, scaled by the average daytime incoming solar radiation (SW_{in}). The daily temperature difference (ΔT) was obtained by subtracting the mean surface temperature averaged between 04:00–06:00 from that averaged between 13:00–15:00. Equation 1 derives from a first-order Fourier approximation, where A_1 and b are the harmonic coefficients, assuming a sinusoidal behaviour of surface temperature (Maltese et al., 2013). The formulation accounts for solar geometry and the phase lag between incoming radiation and surface temperature: ω is the Earth's angular velocity [rad s^{-1}] and δ_1 is the phase shift, which is readily estimated from the timing of the daily temperature maximum.

APs was computed daily using meteorological data collected by the AWSs of Cime Bianche and Torgnon over the five winter seasons from 2016 to 2021.

2.3 Radar backscattering data

2.3.1 Sentinel-1

The Sentinel-1 (S1) data has been used to estimate the snow melting phases in the 2016–2021 period. S1 constellation consists of two satellites offering a revisit time of 6 days. These satellites capture dual polarimetric C-band (5.405 GHz) SAR images. Sentinel-1 Level-1 Ground Range Detected (GRD) images acquired in VV polarization were used to estimate snowmelt phases over the 2016–2021 period. The time series were extracted from the Google Earth Engine (GEE) Sentinel-1 collection, after the standard preprocessing implemented in GEE. For each site, the Sentinel-1 backscatter signal was extracted from a 10 × 10 pixel window centred on the AWS location. Given the 10 m pixel spacing of the Sentinel-1 products in GEE, this window corresponds to an approximate spatial support of 100 × 100 m. To reduce speckle while preserving the temporal evolution of the local backscatter signal, the extracted Sentinel-1 time series were processed using the multitemporal despeckling approach of Quegan and Yu (2001). This filtering procedure reduces the variance associated with speckle while preserving the local mean backscatter. Therefore, the resulting signal should not be interpreted as a simple spatial average of a homogeneous 100 × 100 m area, but rather as a locally representative, despeckled backscatter time series around the AWS.

Level-1 Ground Range Detected (GRD) data (Carletti et al., 2025) with a co-polarized VV (vertical-vertical) signal and spatial resolution of 20 m are used. The time-series are extracted from Google Earth Engine (GEE). Additionally to the pre-processing applied by GEE, an average over a window of 10 × 10 pixels is taken and a multitemporal de-speckling filter is applied. We considered all available tracks acquired both in the morning and in the afternoon, i.e., T88 (17:22 UTC), T66 (5:34 UTC) and T139 (5:43 UTC).

2.3.2 COSMO-SkyMed

The COnstellation of small Satellites for Mediterranean basin Observation (COSMO-SkyMed) is an Earth observation mission funded by the Italian Space Agency and the Italian Ministry of Defence (Covello et al., 2010). The first-generation constellation consists of four medium-sized satellites in sun-synchronous low Earth orbit at an altitude of approximately 620 km (Pettinato et al., 2013). Each satellite is equipped with a multi-mode, high-resolution SAR operating in the X-band (9.6 GHz) (Covello et al., 2010). The HH (Horizontal-Horizontal) signal has been used on this study.

Over the study area, COSMO-SkyMed provides acquisitions from both ascending and descending orbits, resulting in an effective revisit time of approximately 8 days, while each individual orbital track has a nominal revisit interval of about 16 days. In this work, we refer to the two acquisition geometries as orbit A (ascending ≈04:59 UTC) and orbit D (descending ≈17:32 UTC). We used these orbits because they were the only two available for our study area.

The COSMO-SkyMed data were processed in SARScape using multilooking, Frost despeckling and then geocoding using a digital elevation model (DEM). The processed images, with a pixel size of 10 × 10 m, were collected in a single co-registered stack to facilitate multitemporal comparison and backscatter coefficient extraction.

The potential of existing X-band SAR missions for retrieving snow properties (e.g., SWE and snow depth) has been demonstrated in prior studies (Pettinato et al., 2013; Santi et al., 2022). The X-band frequency is especially sensitive to the water content and microstructure of the snowpack, producing stronger electromagnetic interactions than C-band in snow contexts (Santi et al., 2022). In this work, COSMO-SkyMed time series (X-band) are compared to Sentinel-1 (C-band) observations for the 2017/2018 season to highlight similarities and differences in their microwave responses during snowmelt.

2.4 SNOWPACK simulations

The SNOWPACK model, developed by the WSL Institute for Snow and Avalanche Research SLF, considers 1-D partial differential equations governing mass, energy, and momentum conservation, addressing heat transfer, water transport, vapor diffusion, and mechanical deformation in a three-component snowpack (ice, water, and air) (Bartelt and Lehning, 2002). Meteorological data, obtained from *in situ* measurements, serve as input and MeteoIO is used for preprocessing (filtering, gap-filling, and generation of missing parameters). Surface energy exchange was simulated using SNOWPACK's physically based surface energy-balance formulation. Measured incoming and reflected shortwave radiation and measured incoming longwave radiation were used as radiative forcing, while conductive heat transfer within the snowpack was solved by the model's multilayer heat-transfer scheme. The snowpack upper boundary condition was constrained using measured snow surface temperature. Regarding the atmospheric stability, the Monin-Obukhov parametrization is applied. The liquid water transport in the snow and soil is modelled by using the Richards equation. The model assumes a constant ground temperature. Fresh snowfall is usually determined by subtracting model snow depth from measured snow depth, considering reliable humidity and temperature conditions. However, given the absence of reliable snow depth measurements in Cime Bianche, the snowfall is determined by considering the precipitation input for that station. The simulations have been conducted with the typical time step of 15 min in the same period of APs and S1 data. The only calibration parameter considered in the simulations was the aerodynamic roughness length. This parameter was calibrated by maximizing the agreement between simulated and observed SWE at the Torgnon test site, resulting in a selected value of 0.002 m. This value resulted in an average Pearson correlation 0.95 and an average bias of 27 mm over the analyzed time frame. As SWE measurements were not available at the Cime Bianche site, the same parameterization was adopted without further calibration.

We consider the first 40 cm of the snowpack for modelling temperature, LWC, and SWE, following the definition of snow melting phase in Colombo et al. (2019).

2.5 Snow melting phases detection

In this study, we propose three sets of rules for the detection of snow melting phases. Each set is based on one of the three datasets used in this study: AWS and APs data, S1 backscattering data, and SNOWPACK simulations. Snowmelt dates were identified based on the dataset and for each data source, thresholds were defined. These thresholds were established following the state of the art from previous studies and, they represent a first step toward the formalization of snowmelt process.

2.5.1 AWS - APs data

During the accumulation period, the snowpack is primarily composed of dry snow, characterized by high albedo values and large diurnal fluctuations in surface temperature. These characteristics result in low apparent thermal property (APs) values. As air temperature increases, the snowpack undergoes metamorphism, driven by decreases in both albedo and surface temperature variability. This process corresponds to an increase in APs values. The warming phase is identified when APs values begin to rise following the accumulation period, typically exhibiting mean values in the range of 100–200 J m^{-2} K^{-1} $s^{-½}$. The onset of the ripening phase is defined when APs values exceed 500 J m^{-2} K^{-1} $s^{-½}$, a threshold representing the transition from dry to wet snow. During ripening, APs values continue to increase until reaching a maximum, signalling the output phase. During the melting period, decreases in APs values can be attributed to late snowfall events or reductions in snow temperature leading to refreezing of LWC. The end of the output phase is defined when snow depth falls below 5 cm. This threshold, based on point measurements, is considered representative of the area, as snow distribution becomes patchy at this stage, with some zones already snow-free and others retaining minimal snow.

2.5.2 Radar backscattering data

Snowmelt phases are identified by exploiting the complementary information provided by morning and afternoon multitemporal SAR backscattering series (Marin et al., 2020). The onset of the melting phase can be detected when the afternoon backscattering signal shows a decline of at least 2 dB compared to the overall winter baseline. This behaviour is associated with the first appearance of liquid water within the snowpack (Nagler and Rott, 2000). The transition to the ripening phase occurs when a similar decrease of 2 dB is also observed in the morning backscattering time series, indicating that the snowpack has reached an almost isothermal condition. During this period, the backscattering continues to decline. The ripening phase ends when both morning and afternoon signals converge toward their respective local minima (computed as the average of the minima across the three different Sentinel-1 tracks). In this study, this condition serves as an operational indicator of the transition from the ripening phase to the runoff phase. However, we note that the SAR local minimum should not be interpreted as direct evidence of runoff onset (Carletti et al., 2025). While a saturated snowpack expectedly causes strong signal attenuation via liquid water, surface roughness contributions only kick in once sun cups begin to develop. Consequently, the SAR signal is sensitive to mechanisms that do not constitute a direct observation of runoff. Although these processes occur close to the onset of runoff, several factors—such as snow microstructure, melt–refreeze crusts, surface roughness, and local snowpack heterogeneity—may introduce uncertainty. The subsequent runoff phase is generally characterized by a progressive recovery of backscatter toward accumulation-period values. This increase is interpreted as a result of increasing surface roughness combined with the progressive development of a patchy snow cover toward the end of the melt season.

This approach has been evaluated on C- and L-band radar data (Lodigiani et al., 2025), confirming its suitability for detecting snowmelt phases in both S-1 and COSMO-SkyMed time series.

Because Sentinel-1 observations are discrete in time, SAR-derived transition dates have an intrinsic uncertainty related to the revisit interval. For an individual relative orbit, the nominal revisit time is approximately 6 days. Therefore, the timing of a detected transition should be interpreted with an uncertainty of 6 days. This uncertainty was considered when comparing SAR-derived phase dates with daily APs estimates and SNOWPACK simulations, which have finer temporal resolution and discussed in Section 4.3.

2.5.3 SNOWPACK simulations

The warming phase is defined as the period during which snowpack temperatures increase from the low values typical of the accumulation season until reaching 0 °C. As spring approaches and solar radiation intensifies, temperatures rise progressively, producing a characteristic ramp that ends at the isothermal condition of 0 °C. This transition marks the completion of the warming phase. Once the snowpack becomes isothermal, temperature measurements no longer allow a clear separation between the ripening and output phases. For this reason, other parameters are used to identify the subsequent phases. The ripening

TABLE 1 **Criteria used to identify the three main snowmelt phases (warming, ripening, and output) from different datasets, presented as a first step toward the formalization of phase-detection rules.**

Method	Warming	Ripening	Output
AWS - APs	The APs starts to increase after the accumulation period, with values general ranging between 100–200 $Jm^{-2}K^{-1}s^{-\frac{1}{2}}$	The APs values exceed the threshold of 500 $Jm^{-2}K^{-1}s^{-\frac{1}{2}}$	The highest peak indicates the output phase. The end of this phase is determined when snow depth falls below 5 cm
Radar backscattering (S1 - VV)	The warming phase starts when the multitemporal SAR signal recorded in the afternoon decreases by ≥ 2 dB compared to the general accumulation period	The ripening phase begins when morning backscattering signals also decrease by ≥ 2 dB. During this phase, both morning and afternoon signals show a sharp decline until reaching their local minimum	The mean date of the local minima of the three signals marks the onset of the output phase, characterized by a monotonic increase in the backscattering coefficient
SNOWPACK model data	Surface temperature shows a steady increase, reaching 0 °C at the end of the phase	Initiated when LWC reaches 1 mm; melt begins but is fully retained in the snowpack	The decrease in SWE defines the output phase and coincides with the onset of runoff. The end of the phase is reached when snow depth is < 5 cm

For apparent thermal inertia of snow (APs), phase detection applies fixed thresholds; for Sentinel-1 SAR backscattering, changes in signal intensity relative to the winter trend are used; and for the SNOWPACK model, snowpack temperature, liquid water content (LWC), and snow water equivalent (SWE) provide phase delineation.

phase begins when LWC attains 1 mm, indicating the onset of melt; in this interval, all meltwater remains stored within the snowpack. The decline of SWE provides evidence for the beginning of the release of liquid water and thus of the output phase. The end of the output phase is determined from snow depth measurements: a value below 5 cm is taken to indicate its conclusion, consistent with the justification previously provided in Section 2.5.1.

The three set of rules explained above are summarized in Table 1.

2.6 Comparison of snow melting phases detection with the three methods

The estimated day of year (DOY) of the onset of different snow melting phases was compared among the three methods analysed in this study. Four metrics were calculated to compare the different DOY: the coefficient of determination (R^2), the Bias (also referred to as Mean Error), the Root Mean Square Error (RMSE) and the Mean Absolute Error (MAE). This set of metrics is able to assess not only the shared variance but also the agreement in days per phase and per site.

3 Results

In this section, we describe the temporal trends of APs, S1, and the SNOWPACK model, from which the phases were derived according to the criteria outlined in Section 2.5. We first present a focus on results from the 2017/2018 hydrological season for all three methods of snow melting phase detection. Results of all hydrological seasons are provided as Supplementary Figures S1–S5. Finally, a comparative analysis of the results obtained using the different approaches is presented for the whole period considered in this study (i.e. 2016-2021).

3.1 Temporal trends of snow phases for the 2017–2018 season

The three datasets were first analysed separately to estimate the onset and conclusion of the three melting phases. In a subsequent step, the results were compared across datasets on an equal basis. In a subsequent step, the results were compared across datasets as a three-way intercomparison of complementary methods, each based on physically distinct principles and sensitive to different aspects of the snowmelt process. No independent field observations were available at either site; therefore, no method is treated as ground truth, and the analysis focuses on mutual consistency and physical interpretation of the observed offsets.

3.1.1 Apparent thermal inertia - APs

During this winter season, snow depth exceeded 1.5 m at both sites, as illustrated in Figures 3C,D. Cime Bianche site is characterized by strong winds (Pogliotti et al., 2015), thus the snow depth series feature a typical seesaw behaviour, which is not observed at Torgnon. At Cime Bianche (Figures 3A,C), a brief warming phase occurred in early April, followed by a prolonged and variable ripening phase that lasted until mid-June. The output phase, marked by the maximum APs peak, was recorded in the second half of June. In Torgnon, APs values remained stable until mid-April, when it crossed the 500 J m^{-2} K^{-1} $s^{-1}/^{2}$ threshold, indicating the onset of the ripening phase (Figure 3B). A sharp increase in early May, from 500 to 1500 J m^{-2} K^{-1} $s^{-1}/^{2}$, defined the output phase. A subsequent late snowfall caused a temporary drop in APs values, followed by a renewed increase that highlighted the melting of the last remaining snow.

3.1.2 Sentinel-1 backscattering time series

At Cime Bianche (Figure 4A), the warming phase begins in mid-April, when the afternoon backscatter signal from orbit 88 starts to

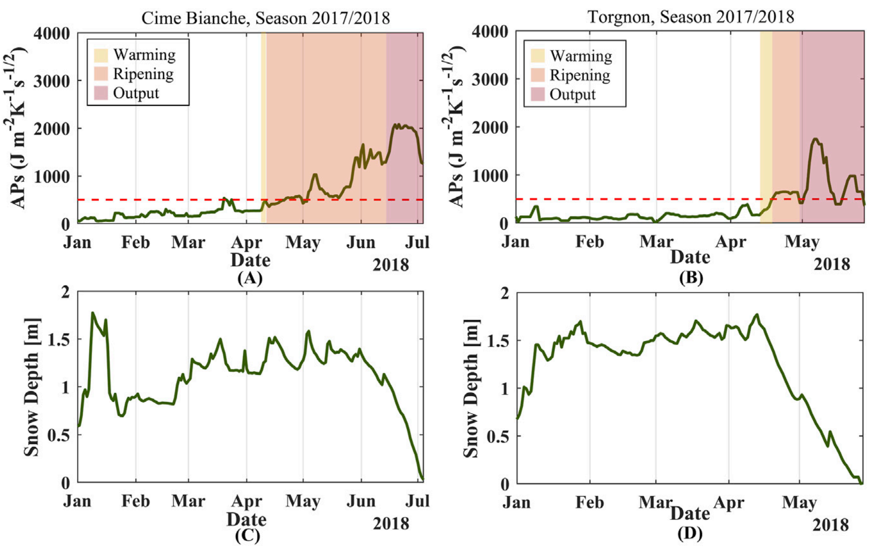

FIGURE 3
Seasonal Evolution of apparent thermal inertia and snow depth at the Alpine site Cime Bianche **(A,C)** and the sub-Alpine site Torgnon **(B,D)** during 2017/2018 season. Panels **(A,B)** show daily APs values (dark green lines), with the red dashed line indicating the APs threshold of 500 J m^{-2} K^{-1} s$^{-1/2}$ used to mark the onset of the ripening phase. Coloured shading highlights the three snowmelt phases: warming (yellow), ripening (orange), and output (red). Panels **(C,D)** display corresponding snow depth time series, used to determine the end of the output phase when snow depth falls below 5 cm.

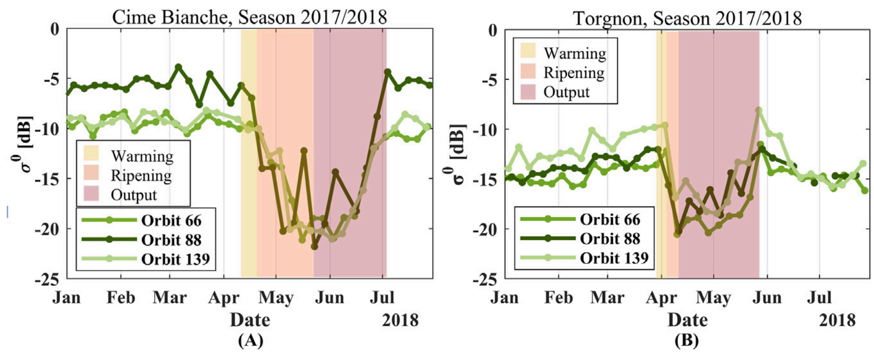

FIGURE 4
Seasonal evolution of Sentinel-1 backscattering at Cime Bianche **(A)** and Torgnon **(B)** during the 2017/2018 season. Both panels show time series of SAR backscatter for orbits 66, 88, and 139. Coloured shading indicates the three snowmelt phases: warming (yellow), ripening (orange), and output (red).

decrease, followed shortly afterwards by orbits 66 and 139. In this way, the onset of the warming phase is marked by the initial decline of the afternoon signal, while its end is reached once the morning backscatter signals (orbits 66 and 139) also begin to decrease. A sharp drop of about −10 dB then emphasizes the transition into the ripening phase, which lasts for 32 days from 21 April to 23 May. The subsequent output phase is more irregular, with alternating intervals of increasing and decreasing backscatter, although the timing of transitions remains consistent among the three orbits. Overall, the output phase extends from 24 May to 5 July, reflecting a gradual recovery of the backscatter signal through the end of the melting season.

At Torgnon (Figure 4B), the backscatter signal shows greater variability among the three orbits compared to Cime Bianche. During the accumulation period between January and March, the C-band penetrates the dry snowpack, producing relatively stable values of about −15 dB. A short warming event from 30 March to 3 April causes only limited fluctuations, but this is followed by a marked decrease during the ripening phase, which lasts for approximately 18 days. The output phase is more irregular and discontinuous: orbit 66 displays a gradual recovery of the backscatter signal extending into late May, orbit 88 alternates between freezing and melting cycles with corresponding oscillations in backscatter, while orbit 139 reaches its minimum in early May before showing an increase. According to the criteria reported in the literature, the onset of the output phase is identified by averaging the three local minima, which in this case corresponds to 23 April. The melting process is considered complete once the backscatter values consistently rise again, a transition that occurs on 27 April. Overall, the Torgnon site is characterized by a more heterogeneous and variable output

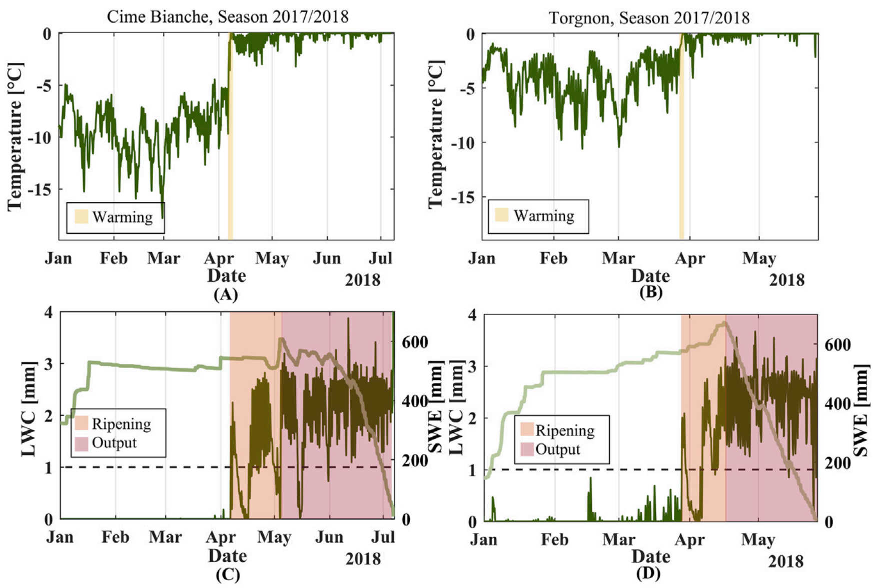

FIGURE 5
Seasonal evolution of modelled snowpack properties from SNOWPACK model at Cime Bianche **(A,C)** and Torgnon **(B,D)** during 2017/2018. Panels **(A,B)** show surface temperature, with the yellow shading marking the warming phase. Panels **(C,D)** display LWC (left axis, dark green lines) and SWE (right axes, light green lines). The ripening phase (orange shading) is defined by LWC values exceeding 1 mm, while the output phase (red shading) occurs when SWE starts to decrease, until snow depth falls below 5 cm.

phase, highlighting the orbit-dependent response of the snowpack to melting and refreezing conditions.

3.1.3 SNOWPACK simulations

The warming phases were clearly identified by the temperature ramp from negative values to 0 °C. At Cime Bianche (Figure 5A), temperature increased from −10 °C to 0 °C in 3 days (5–8 April), while at Torgnon (Figure 5B) it rose from −4 °C to 0 °C in 4 days (26–30 March). At both sites, the period during which LWC exceeded the 1 mm threshold - marking the development of the ripening phase - extended from 8 April to 5 Ma y at Cime Bianche and from 28 March to 16 May at Torgnon. The onset of the output phase was then identified by SWE beginning to decline, indicating the release of liquid water from the snowpack (Figures 5C,D). At Cime Bianche, SWE remained stable at 500–600 mm until early May, after which it gradually decreased. At Torgnon, the output phase began in mid-April and was characterized by a steady decline in SWE, with complete snow disappearance on 26 May. For the 2017–2018 season at Torgnon, all three datasets (APs, SAR backscatter, and SNOWPACK) consistently indicated the end of the output phase between 26 and 29 May.

3.2 Comparison of snow melting phases from different methods

In this section, we compare the onset of the three melting phases (warming, ripening, and output) as estimated by the three approaches. In Table 2, we present the site- and phase-specific agreement of snow melting phase detection for Torgnon and Cime Bianche,The agreement is here evaluated in terms of R^2, Bias, RMSE and MAE.

While a general good agreement was found among different estimates at the two sites, some comparisons yielded low statistics. In particular, the warming phase showed the lowest R^2 values among the three phases in most method pairs and at both sites, with values ranging from 0.09 (Sentinel-1–SNOWPACK, Cime Bianche) to 0.88 (APs–SNOWPACK, Torgnon). The comparison between Sentinel-1 and SNOWPACK was particularly weak for this phase at both sites (R^2 = 0.21 at Torgnon and 0.09 at Cime Bianche).

The ripening phase generally showed higher agreement than warming across method pairs, reaching its highest value for APs–Sentinel-1 at Cime Bianche (R^2 = 0.95). At Torgnon, however, Ripening agreement remained comparatively low for the Sentinel-1–SNOWPACK pair (R^2 = 0.23), mirroring the pattern already observed for Warming at this site.

The output phase displayed the widest range of results across method pairs and sites. At Torgnon, it was the best-performing phase overall, with R^2 = 0.98 for APs–Sentinel-1 and R^2 = 0.69 for Sentinel-1–SNOWPACK. At Cime Bianche, by contrast, Output showed the lowest R^2 of the entire dataset for APs–SNOWPACK (R^2 = 0.09, MAE = 41 days) and a low value for APs–Sentinel-1 (R^2 = 0.31), despite very low absolute errors (RMSE = 1 day, MAE = 23 days); the Sentinel-1–SNOWPACK pair, however, performed comparatively well for this phase at the same site (R^2 = 0.79).

Figure 6 shows the DOY of onset and termination of each phase derived from APs and from SNOWPACK simulations. Cime Bianche and Torgnon are represented by circles and triangles, respectively, with colours indicating the different phases (yellow = warming, orange = ripening, red = output). Most points lie

TABLE 2 Statistical metrics between the three methods used to detect snow melting phase onsets - APs, Sentinel-1 SAR backscattering (S1), and the SNOWPACK model - at Torgnon and Cime Bianche for the Warming, Ripening, and Output phases over the five winter seasons (2016–2021).

TORGNON	APs vs. Sentinel-1				APs vs. SNOWPACK				Sentinel-1 vs. SNOWPACK			
	R^2	Bias	RMSE	MAE	R^2	Bias	RMSE	MAE	R^2	Bias	RMSE	MAE
Warming	0.37	33	14	23	0.88	9	18	7	0.21	−24	4	16
Ripening	0.56	29	15	29	0.83	7	20	15	0.23	−22	5	14
Output	0.98	9	8	13	0.59	10	15	31	0.69	1	7	18
CIME BIANCHE	APs vs. Sentinel-1				APs vs. SNOWPACK				Sentinel-1 vs. SNOWPACK			
	R^2	Bias	RMSE	MAE	R^2	Bias	RMSE	MAE	R^2	Bias	RMSE	MAE
Warming	0.35	26	4	3	0.62	21	8	3	0.09	−5	12	6
Ripening	0.95	5	3	9	0.76	23	7	4	0.60	18	4	13
Output	0.31	−2	1	23	0.09	13	5	41	0.79	15	6	18

For each pairwise comparison, the coefficient of determination (R^2), Bias (days), root mean square error (RMSE, days), and mean absolute error (MAE, days) are reported. Positive bias values indicate that the first method detects the phase onset later than the second.

close to the 1:1 line (R^2 = 0.91) indicating a high correlation between the two methods. The regression line lies slightly below the equality line, showing that APs typically detects phase onsets later than the model. APs delays the warming phase by a small margin, while the ripening phase shows the closest match between the two approaches. The output phase exhibits the largest variability, with APs sometimes preceding and sometimes lagging the SNOWPACK estimates. Phase-specific regressions support these findings, with R^2 = 0.95 for warming, 0.96 for ripening, and 0.86 for output.

The melting phases at Torgnon occur between DOY 60–150, whereas at Cime Bianche they fall between DOY 100–190.

Figure 7A shows the comparison between the DOY of snowmelt phases derived from APs and from Sentinel-1 backscattering for orbits 66, 88, and 139. A relatively highcoefficient of determination (R^2) equal to 0.86 is observed. Similar to the comparison with SNOWPACK, warming and ripening phases (yellow and orange markers) are generally detected later by APs, as indicated by their position below the 1:1 line. Conversely, for the output phase, APs sometimes precedes the onset relative to SAR-derived estimates.

The melting phases in Torgnon occur earlier (DOY 60–160, March–June) compared to Cime Bianche (DOY 100–200, April–July).

Figure 7B shows the comparison between the DOY of snow phases estimated from Sentinel-1 backscatter data and those derived from the SNOWPACK model. This comparison reveals a high correlation between the two datasets (R^2 = 0.91). The initial portion of the regression line closely overlaps the 1:1 line, indicating that the onset of the different snow phases, occurring between DOY 60 and 100, is consistently estimated by both methods. In contrast, the final portion of the regression line lies above the 1:1 line, suggesting that the end of the output phase, and therefore the end of the melting season, is estimated slightly later when using Sentinel-1 backscatter data compared to the SNOWPACK model.

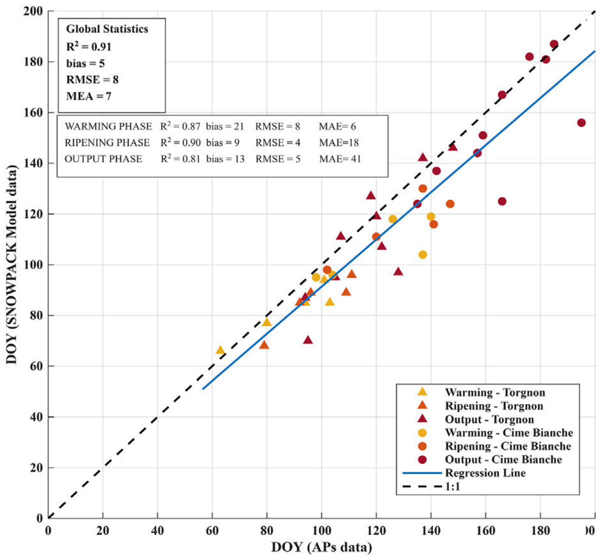

FIGURE 6
Comparison between DOY of snowmelt phases estimated from APs and SNOWPACK simulations at Cime Bianche and Torgnon over the 2016–2021 period. For each season, four points are shown: yellow symbols mark the onset of the warming phase, orange symbols the onset of the ripening phase, and red symbols the onset and end of the output phase. Symbols distinguish the two sites (circles = Cime Bianche; triangles = Torgnon). The dashed line represents the 1:1 relationship, and the solid blue line shows the overall regression fit (R^2 = 0.91). Phase-specific regression lines and coefficients of determination are reported in the inset, together with bias, RMSE, and MAE for both the overall and phase-specific comparisons.

3.3 Comparing the temporal evolution of APs and backscattering S1 signals

Figure 8 illustrates the seasonal evolution of APs (Figure 8A) and Sentinel-1 backscatter (σ^0) (Figure 8B) for a representative winter (2017/2018) at Cime Bianche and Torgnon.

10.3389/feart.2026.1869925

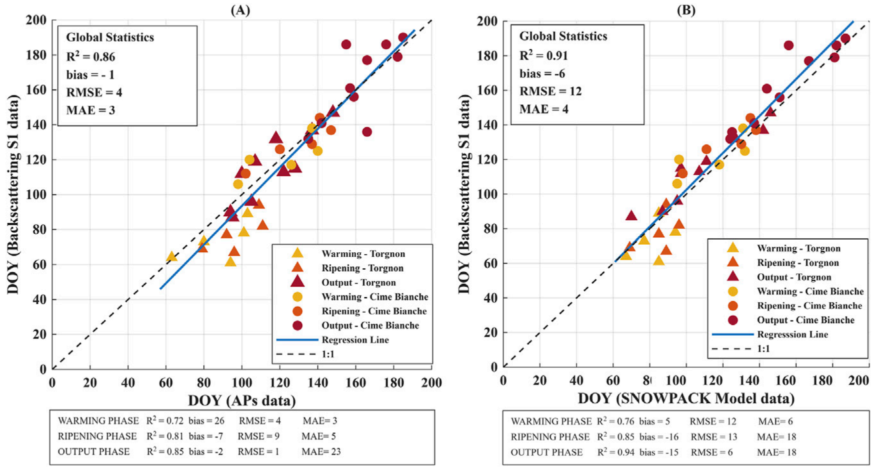

FIGURE 7
Comparison of the DOY of snowmelt phases derived from Sentinel-1 backscattering with **(A)** APs and **(B)** SNOWPACK simulations at Cime Bianche (circles) and Torgnon (triangles) over the 2016–2021 period. Colours indicate the three phases: warming (yellow), ripening (orange), and output (red). The dashed line represents the 1:1 relationship, while solid lines show linear regressions between datasets. Phase-specific regressions with coefficients of determination (R^2) are reported in the inset boxes, along with bias, RMSE, and MAE for both the overall and phase-specific comparisons.

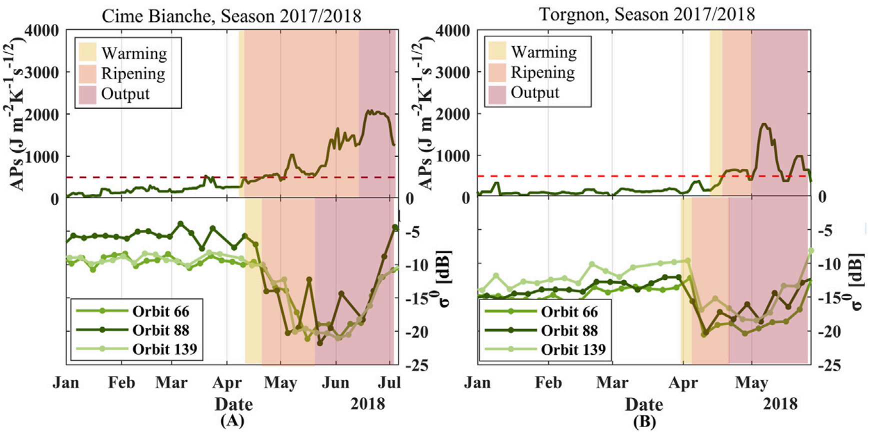

FIGURE 8
Comparison between the seasonal evolution of apparent thermal inertia (APs, upper panels, left axis) and Sentinel-1 backscatter coefficient σ° (lower panels, right axis) at Cime Bianche **(A)** and Torgnon **(B)** for the reference season 2017/2018. For backscatter, results from the three Sentinel-1 acquisition orbits (66, 88, 139) are shown. Coloured shading highlights the three snowmelt phases: warming (yellow), ripening (orange), and output (red). These examples illustrate the consistency between APs-derived and SAR-derived detection of the melting phases at both sites.

At both sites, APs values remain low and relatively stable during winter (January–March), indicating limited melt activity. In early spring, a marked increase in APs is observed. At Cime Bianche, APs start to rise in late April and increase progressively through May and June, reaching peak values in early summer. A similar pattern is observed at Torgnon, with a sharp increase occurring in April followed by sustained elevated values during May. The S1 backscattering time series show a contrasting seasonal evolution. During winter, backscatter remains relatively stable. With the onset of melt conditions in spring, σ^0 exhibits a pronounced decrease, reaching minimum values during the main melt period. At Cime Bianche, this decline begins in late April and persists through May, while at Torgnon a comparable drop occurs in April. After the main melt phase, σ^0 values show partial recovery toward early summer.

Overall, both APs and σ^0 clearly indicate the transition from winter to melt conditions at both study sites. The timing of the seasonal transition is consistent between the two variables, with increasing APs coinciding with decreasing σ^0 during the melt period.

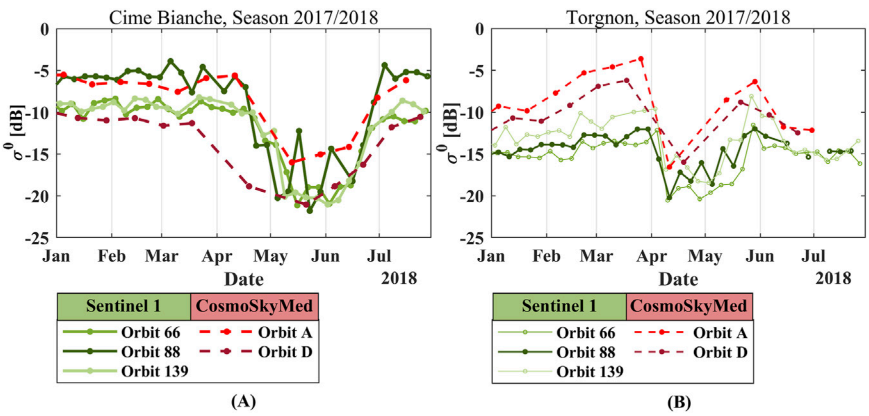

FIGURE 9
Temporal evolution of the radar backscattering coefficient (σ^0, in dB) from Sentinel-1 (C-band, solid lines) and COSMO-SkyMed (X-band, dashed lines) over **(A)** Cime Bianche and **(B)** Torgnon during the 2017/2018 snow season. Sentinel-1 data correspond to orbits 66, 88, and 139, while COSMO-SkyMed acquisitions refer to orbit A and orbit D. The time series highlight the temporal dynamics of the radar response associated with snow accumulation and melting processes.

3.4 Comparing the temporal evolution of two radar signals: Sentinel-1 and cosmo sky-med

The radar backscattering time series reveal a consistent seasonal pattern in both C-band (Sentinel-1) and X-band (COSMO-SkyMed) observations over the Cime Bianche and Torgnon sites during the 2017/2018 season (Figures 9A,B). In both datasets, a clear reduction in σ^0 values is observed during late spring, corresponding to the onset and evolution of the early phases of the snowmelt process, followed by an increase in early summer - output phase - that continues until the complete disappearance of the snow cover.

It should be noted that this comparison is limited to a single hydrological season and is qualitative in nature: no formal phase extraction or agreement metrics, analogous to those derived for Sentinel-1 in Section 2.5.2 and Section 3.2, were computed for COSMO-SkyMed. Furthermore, the two datasets differ not only in operating frequency but also in polarization (VV for Sentinel-1, HH for COSMO-SkyMed), acquisition geometry, and acquisition time, all of which can independently influence the timing and sharpness of the backscatter coefficient. As such, any differences observed between the two time series cannot be unambiguously attributed to wavelength alone, and should be interpreted as a preliminary, descriptive comparison rather than a quantitative validation of one sensor against the other.

4 Discussion

4.1 Overall agreement between methods

The comparison of phases onsets across the three approaches demonstrates a consistently overall agreement, despite their different physical bases and observational characteristics. The high coefficients of determination (R^2 = 0.91 for APs - SNOWPACK, 0.86 for APs - Sentinel-1, and 0.91 for Sentinel-1 - SNOWPACK) indicate that all methods capture the seasonal progression of melt in a coherent manner. This agreement is particularly evident in the clustering of points along the 1:1 line, and relatively low RMSE (ranging from 4 to 12), MAE (ranging from 3 to 7), and Bias (ranging from −6 to 5). In particular, RMSE values obtained for the pooled comparison fall below 9% of the total data variability.

As for the APs and SNOWPACK comparison (Figure 6), the strongest correspondence is observed for the warming and ripening phases, which show high phase-specific R^2 values and limited dispersion around the regression lines. These phases represent sustained and progressive transitions in snowpack energy and liquid water content, making them detectable by thermodynamic modelling and surface radiative metrics. The output phase, in contrast, exhibits greater variability, reflecting the increased influence of short-term meteorological fluctuations, intermittent snowfall events, and internal snowpack heterogeneity near the end of the melt season.

As for the comparison of Sentinel-1 with APs and SNOWPACK (Figure 7), we observed a higher correlation for the Ripening and Output with respect to the Warming phase. This pattern reflects the sensitivity of C-band SAR backscatter to the onset and increase of free liquid water content, which becomes more pronounced and detectable as melt progresses toward ripening and output, rather than to the gradual thermal changes that characterize the warming phase.

Overall, the high level of agreement confirms that, although small systematic offsets exist, the three methods converge in defining the same temporal window of melt evolution. This robustness across independent approaches strengthens confidence in the reliability of the phase detection framework and supports the use of combined modelling and remote sensing techniques for monitoring snowmelt dynamics in Alpine environments.

4.2 Differences in phase onset among methods

The discrepancies in the detected onset of different phases among SNOWPACK, APs, and Sentinel-1 backscatter primarily reflect their different physical sensitivities and conceptual foundations. SNOWPACK, based on an energy-balance framework, identifies the beginning of the warming phase as soon as snow temperature approaches 0 °C. This thermodynamically driven definition explains the systematic earlier detection of melt onset relative to the other approaches and confirms SNOWPACK as the earliest detector among the three methods.

The observed systematic delay between APs and SNOWPACK, is consistent with this behaviour. Since APs is primarily controlled by changes in surface radiative balance and thermal variability, especially reductions in albedo and increased energy absorption, its rise typically occurs after the initial temperature-based signal. As a consequence, APs tends to detect the warming phase slightly later than SNOWPACK (see Table 2). Nevertheless, the relatively small and consistent offsets across seasons indicate that APs provides a stable and robust proxy for identifying the onset of warming, especially in years without significant late snowfall or pronounced melt-refreeze interruptions.

In contrast, Sentinel-1 backscatter shows pronounced interannual variability and does not exhibit a consistent lead or delay relative to SNOWPACK. Unlike APs, which is primarily governed by surface radiative and thermal conditions, SAR backscatter is sensitive to variations in liquid water content within the snowpack, including intermediate and deeper layers. Consequently, the timing of melt detection depends on how meltwater percolates and redistributes vertically, a process that can vary substantially between seasons. This sensitivity explains the large discrepancies observed in years affected by recurrent snowfall events and repeated melt-refreeze cycles, such as 2019/2020, when intermittent "stop-and-go" melting altered the internal snow structure and delayed or disrupted the microwave response.

Overall, while agreement at the phase-onset scale is limited, the three approaches provide complementary insights into the melting process. SNOWPACK consistently precedes the thermodynamic initiation of melt, APs offers a temporally stable indicator of surface radiative changes associated with warming and Sentinel-1 captures structural and hydrological transformations within the snowpack. Together, these differences emphasize both the complexity of defining melt onset and the benefit of integrating physically diverse indicators to achieve a more comprehensive characterization of snowmelt dynamics.

A limitation is encountered in the difference between the measured total snow depth and SNOWPACK modelled snow depth. In this study, SNOWPACK was applied to the upper 40 cm of the snowpack, smaller than the total snow depth often observed at the study sites. Therefore, the model results do not represent the full-depth state of the snowpack. However, they provide an estimation of the near-surface snow layer properties, which is the portion of the snowpack impacting the results obtained from the remote-sensing platforms used in this study.

Differences among the three approaches may also arise from their different spatial supports. APs and SNOWPACK are based on point-scale AWS observations, whereas the Sentinel-1 signal represents a local-area response derived from a despeckled Sentinel-1 resolution cell. Although multitemporal despeckling reduces speckle-related variance while preserving the local mean backscatter, it cannot fully remove the effects of sub-pixel heterogeneity, geolocation uncertainty, or spatial variability in snow depth. This scale mismatch is likely more important at Cime Bianche, where wind redistribution and complex local topography produce heterogeneous snow conditions.

4.3 Temporal evolution of APs and SAR signals

Although both datasets clearly capture the seasonal transition from winter to melt conditions, they indicate the onset of the warming, ripening, and output phases at slightly different times. This temporal offset reflects the fundamentally different nature of the two approaches. APs is a model-derived, daily variable driven by meteorological forcing, whereas σ^0 represents discrete SAR observations that are sensitive to snow structure and internal liquid water content.

The differing temporal resolutions further influence this comparison: APs provides a continuous daily signal, while Sentinel-1 acquisitions occur approximately every 6 days per orbit, resulting in non-uniform sampling. Consequently, short-term transitions may be detected at different moments in the two datasets, leading to limited agreement when phase onset is used as the comparison metric.

An additional factor affecting both signals is the evolution of surface roughness during melt. Increasing roughness reduces snow albedo, thereby enhancing APs values, while simultaneously modifying radar scattering mechanisms, which can alter σ^0. This process may contribute to minor deviations or non-synchronous transitions between the two signals.

Despite these phase-scale differences, the overall seasonal behaviour is highly consistent. A sustained increase in APs coincides with a general decline in σ^0, jointly capturing the onset and progression of melt at both sites within the same temporal window. This complementary behaviour highlights the benefit of combining energy-balance modelling with SAR observations for monitoring snowpack evolution in Alpine environments.

4.4 Differences between alpine and Sub-Alpine sites

The comparison between Cime Bianche (Alpine site) and Torgnon (Sub-Alpine site) highlights a clear elevation control on the timing of snowmelt phases. At Torgnon, all three melting phases consistently occur earlier in the season (approximately DOY 60–160), whereas at Cime Bianche they are shifted later (approximately DOY 100–200). This systematic offset reflects the lower elevation and warmer climatic conditions at Torgnon, which promote earlier snowpack warming and melt initiation. Conversely, the higher elevation of Cime Bianche results in delayed energy input, prolonged snow persistence and a later transition through the melting phases.

Despite these differences in absolute timing, the relative agreement among the three methods remains comparable at both sites. The regression patterns and coefficients of determination indicate that the consistency between approaches is not site-dependent, suggesting that the detection framework is robust across contrasting elevation regimes.

However, the broader DOY range observed at the Alpine site suggests greater sensitivity to interannual variability, likely due to colder baseline conditions and a stronger influence of late-season snowfall events. These factors can prolong the ripening and output phases and introduce short-term interruptions in melt progression. In contrast, the Sub-Alpine site exhibits a more compressed melt season, where transitions between phases occur within a shorter temporal window.

Overall, the observed elevation-dependent shift confirms the dominant role of topography and temperature regime in controlling snowmelt dynamics, while also demonstrating that the combined modelling and remote sensing approaches remain consistent across both Alpine and Sub-Alpine environments.

4.5 Comparison between C-band and X-band radar

The comparison between Sentinel-1 (C-band) and COSMO-SkyMed (X-band) further suggests the potential of multi-frequency SAR for melt detection. Despite the different operating frequencies of the two sensors, the temporal evolution of σ^0 shows a notable agreement, demonstrating that both C- and X-band SAR data are capable of identifying the main stages of the melting process. Small differences can be noted in the amplitude and timing of the σ^0 variations: the X-band signal from COSMO-SkyMed exhibits an earlier and more pronounced decrease, while the C-band signal from Sentinel-1 displays smoother transitions and a slightly delayed response.

Due to its shorter wavelength, the X-band is in principle more sensitive than the C-band to small quantities of liquid water within the snowpack, which could in part explain an earlier response to the moistening of the surface snow layer and a more pronounced loss of interaction with deeper layers as melting progresses (Pettinato et al., 2013). The X-band signal is expected to be more responsive to increases in surface roughness, potentially leading to an earlier detection of the output onset. However, these wavelength-related mechanisms cannot be isolated from other factors that differ between the two datasets. Sentinel-1 and COSMO-SkyMed backscatter differ not only in frequency but also in polarization (VV vs. HH), acquisition geometry and acquisition time, all of which independently influence backscatter sensitivity to surface and volume scattering processes. Consequently, the apparent earlier and sharper response of COSMO-SkyMed should not be attributed to frequency alone, but rather to a combination of physical sensitivity to liquid water, polarization and geometry effects, and the coarser temporal sampling discussed below.

The comparison between the two sensors must also be interpreted in light of their differing temporal sampling. The effective revisit time of COSMO-SkyMed (~8 days, combining ascending and descending orbits) is considerably coarser than that of Sentinel-1, which benefits from improved temporal sampling through the combination of multiple acquisition tracks. Given that the warming phase can last as little as a few days at both sites as observed for instance in the 2017/2018 season (Section 3.1.3), the COSMO-SkyMed sampling interval is of the same order as the duration of this phase itself, raising the possibility that early and short-lived transitions are not fully resolved by the X-band time series. In several instances (e.g., Figure 9B), the backscatter signal from COSMO-SkyMed drops sharply between consecutive acquisitions without a clear gradual precursor, suggesting that the onset of melt may already have occurred between observations. This limitation likely affects the precision with which the warming and ripening phases can be detected using COSMO-SkyMed alone, while the longer-duration output phase would likely remain more robustly identifiable. As such, part of the apparent earlier X-band response discussed above may reflect under-sampling rather than an exclusively physical effect of wavelength.

Overall, the comparison shows that both radar bands capture the seasonal evolution of the snowpack and provide broadly consistent information on the timing and dynamics of snowmelt. However, given the single-season, qualitative nature of this comparison and the confounding influence of polarization, geometry, and temporal sampling, these results should be regarded as a preliminary indication of the complementary potential of multi-frequency SAR for cryospheric monitoring, rather than a definitive validation of differential sensitivity between C- and X-band.

Recent work has shown that dual-polarization Sentinel-1 metrics can improve snowmelt or runoff-onset mapping in complex terrain (Darychuk et al., 2025). This is particularly relevant for spatially distributed applications where terrain, vegetation, and snowpack heterogeneity vary strongly within a basin. In this study, however, we prioritized a single, consistent VV-based time series because the goal was to compare SAR-derived phase dates with daily APs and 1-D SNOWPACK simulations at two AWS sites. Future work should test whether combining VV and VH, or using polarization ratios such as VH/VV, improves the robustness of phase detection when extending the approach from point-scale site analysis to distributed mountain-scale mapping.

5 Conclusion

This study evaluated the combined use of microwave remote sensing (C-band SAR), apparent thermal inertia and physically based modelling (SNOWPACK) to characterize snowmelt dynamics in Alpine environments. Together, these complementary observations consistently identified the three melt phases - warming, ripening, and output - across multiple seasons and sites.

Despite intrinsic spatial and temporal differences among datasets, their temporal alignment proved robust, although the level of agreement varied depending on the melt phase and the site considered, with the Warming phase generally showing the weakest correspondence across methods. Driven by surface temperature and by albedo variations linked to surface roughness and energy-balance conditions, APs effectively detected the onset of the warming phase. In contrast, radar backscatter - sensitive to liquid water and structural changes throughout the snowpack - can precede or lag this surface transition depending on wetting at depth. This distinction highlights the value of combining surface-focused and volume-sensitive indicators.

Our results further confirm that snowmelt is a gradual and often intermittent process, with late snowfall or cooling events temporarily restoring dry conditions, challenging the use of fixed thresholds. Differences of 4–12 days (2.9%–8.9% of the total variability) are not negligible for operational runoff forecasting, particularly in rapidly responding mountain catchments. Although an error in detected melt onset does not necessarily translate directly into an equivalent error in peak-runoff timing because peak flow also depends on SWE, subsequent meteorological forcing, rainfall and catchment routing it can affect the timing of simulated meltwater input and reservoir characteristics. Our phase estimates are currently more suitable for seasonal monitoring, model evaluation and data assimilation than as standalone predictors of peak runoff. Their timing uncertainty should be explicitly propagated when they are used in hydrological forecasting and water-management applications.

Finally, both Sentinel-1 (C-band) and COSMO-SkyMed (X-band) reliably captured seasonal snow evolution. X-band responded more sharply and earlier to initial surface moistening, whereas C-band exhibited smoother and slightly delayed changes due to deeper penetration. These complementary behaviours underscore the potential of multi-frequency SAR for future cryospheric monitoring. Future satellite thermal mission such as the ESA–Land Surface Temperature Monitoring mission and the NASA–Surface Biology and Geology - Thermal Infrared mission will allow an extended monitoring of apparent thermal inertia of snow at high spatial resolution (~50–60 m). This unprecedented opportunity will grant us a deeper understanding of snow melting phases both in midlatitude and polar regions. Further still, novel hyperspectral satellite missions such as PRISMA and EnMAP allow the retrieval of snow properties (e.g., light-absorbing impurities, LWC) useful for the determination of snow melting phases from space (Di Mauro et al., 2024; Ravasio et al., 2024).

Future L-band SAR missions, notably ESA's ROSE-L and the NASA-ISRO NISAR (National Aeronautics and Space Administration-Indian Space Research Organisation Synthetic Aperture Radar) mission, are expected to significantly improve data collection in wet snow conditions. Since L-band signals are less attenuated compared to shorter C- and X-bands, these missions will offer a greater opportunity to accurately retrieve the LWC.

Looking forward, this combined framework could improve snow monitoring strategies in Alpine regions, with implications for hydrological forecasting, water resource management and climate change impact studies. Future work should aim to refine the synergy among remote sensing and modelling by addressing scale mismatches, improving temporal resolution and extending the analysis to larger spatial domains.

Data availability statement

The original contributions presented in the study are included in the article/Supplementary Material. A Python implementation to calculate the apparent thermal inertia of snow from AWS data is provided at https://github.com/LTDA-disat/APs further inquiries can be directed to the corresponding author (biagio.dimauro@cnr.it).

Author contributions

OG: Data curation, Software, Writing – original draft, Formal Analysis. BDM: Data curation, Writing – review and editing, Conceptualization. CM: Data curation, Writing – review and editing, Methodology. RG: Methodology, Software, Writing – review and editing. GB: Formal Analysis, Writing – review and editing. VP: Writing – review and editing, Software, Formal Analysis. CN: Methodology, Writing – review editing. SP: Writing – review and editing, Data curation. CR: Writing – review and editing, Data curation, Software. EC: Writing – review and editing, Data curation, Resources. PP: Data curation, Writing – review and editing, Resources. RC: Writing – review and editing, Conceptualization, Funding acquisition.

Funding

The author(s) declared that financial support was received for this work and/or its publication. This work has been supported by the CRIOSAR ("Applicazioni SAR multifrequenza alla criosfera") project (Grant ASI N. 2021-12-U.0), funded by the Italian Space Agency (ASI).

Acknowledgments

We acknowledge the ARPA (Environmental Protection Agency of the Aosta Valley region) for providing the AWS dataset in Torgnon and Cime Bianche. The Reviewers and Editor are acknowledged for their constructive comments on our manuscript.

Conflict of interest

The author(s) declared that this work was conducted in the absence of any commercial or financial relationships that could be construed as a potential conflict of interest.

Generative AI statement

The author(s) declared that generative AI was not used in the creation of this manuscript.

Any alternative text (alt text) provided alongside figures in this article has been generated by Frontiers with the support of artificial intelligence and reasonable efforts have been made to ensure accuracy, including review by the authors wherever possible. If you identify any issues, please contact us.

Publisher's note

Supplementary material

The Supplementary Material for this article can be found online at: https://www.frontiersin.org/articles/10.3389/feart.2026.1869925/full#supplementary-material

References

Bartelt, P., and Lehning, M. (2002). A physical SNOWPACK model for the Swiss avalanche warning: part I: numerical model. *Cold Regions Sci. Technol.* 35 (3), 123–145. doi: 10.1016/S0165-232X(02)00074-5

Carletti, F., Marin, C., Ghielmini, C., Bavay, M., and Lehning, M. (2025). Multitemporal analysis of Sentinel-1 backscatter during snowmelt using high-resolution field measurements and radiative transfer modelling. *Cryosphere* 19, 5579–5612. doi: 10.5194/tc-19-5579-2025

Colombo, R., Garzonio, R., Di Mauro, B., Dumont, M., Tuzet, F., Cogliati, S., et al. (2019). Introducing thermal inertia for monitoring snowmelt processes with remote sensing. *Geophys. Res. Lett.* 46 (8), 4308–4319. doi: 10.1029/2019GL082193

Colombo, R., Pennati, G., Pozzi, G., Garzonio, R., Di Mauro, B., Giardino, C., et al. (2023). Mapping snow density through thermal inertia observations. *Remote Sens. Environ.* 284, 113323. doi: 10.1016/j.rse.2022.113323

Covello, F., Battazza, F., Coletta, A., Lopinto, E., Fiorentino, C., Pietranera, L., et al. (2010). COSMO-SkyMed an existing opportunity for observing the Earth. *J. Geodyn.* 49 (3–4), 171–180. doi: 10.1016/j.jog.2010.01.001

Darychuk, S. E., Shea, J. M., and Derksen, C. (2025). Comparison of snowmelt timing estimates from Sentinel-1 SAR and surface observations in British Columbia, Canada. *Remote Sens. Environ.* 328, 114863. doi: 10.1016/j.rse.2025.114863

Di Mauro, B., Garzonio, R., Rossini, M., Filippa, G., Pogliotti, P., Galvagno, M., et al. (2019). Saharan dust events in the European alps: role in snowmelt and geochemical characterization. *Cryosphere* 13 (4), 1147–1165. doi: 10.5194/tc-13-1147-2019

Di Mauro, B., Cogliati, S., Bohn, N., Traversa, G., Garzonio, R., Tagliabue, G., et al. (2024). Evaluation of PRISMA products over snow in the alps and Antarctica. *Earth Space Sci.* 11 (7), e2023EA003482. doi: 10.1029/2023EA003482

Dingman, S. L. (2015). *Physical Hydrology*. 3rd Edn. Long Grove, Illinois: Waveland Press, Inc. 643.

Dumont, M., Tuzet, F., Gascoin, S., Picard, G., Kutuzov, S., Lafaysse, M., et al. (2020). Accelerated snow melt in the Russian Caucasus Mountains after the Saharan dust outbreak in March 2018. *J. Geophys. Res. Earth Surf.* 125 (9), e2020JF005641. doi: 10.1029/2020jf005641

Lodigiani, M., Marin, C., and Pasian, M. (2025). Mixed analytical-numerical modeling of radar backscattering for seasonal snowpacks. *IEEE J. Sel. Top. Appl. Earth Observations Remote Sens.* 18, 3461–3471. doi: 10.1109/JSTARS.2024.3521612

Lund, J., Forster, R. R., Deeb, E. J., Liston, G. E., Skiles, S. M., and Marshall, H.-P. (2022). Interpreting Sentinel-1 SAR backscatter signals of snowpack surface melt/freeze, warming and ripening, through field measurements and physically-based SnowModel. *Remote Sens.* 14 (16), 4002. doi: 10.3390/rs14164002

Ma, C., Wang, W., Han, X., and Li, X. (2013). Soil moisture retrieval in the Heihe River Basin based on the real thermal inertia method. *IEEE J. Sel. Top. Appl. Earth Observations Remote Sens.* 6 (3), 1460–1467. doi: 10.1109/JSTARS.2013.2252149

Magnusson, J., Nævdal, G., Matt, F., Burkhart, J. F., and Winstral, A. (2020). Improving hydropower inflow forecasts by assimilating snow data. *Hydrology Res.* 51 (2), 226–237. doi: 10.2166/nh.2020.025

Maltese, A., Bates, P. D., Capodici, F., Cannarozzo, M., Ciraolo, G., and La Loggia, G. (2013). Critical analysis of thermal inertia approaches for surface soil water content retrieval. *Hydrological Sci. J.* 58 (5), 1144–1161. doi: 10.1080/02626667.2013.802322

Marin, C., Bertoldi, G., Premier, V., Callegari, M., Brida, C., Hürkamp, K., et al. (2020). Use of Sentinel-1 radar observations to evaluate snowmelt dynamics in alpine regions. *Cryosphere* 14, 935–956. doi: 10.5194/tc-14-935-2020

Minacapilli, M., Iovino, M., and Blanda, F. (2009). High resolution remote estimation of soil surface water content by a thermal inertia approach. *J. Hydrol.* 379 (3), 229–238. doi: 10.1016/j.jhydrol.2009.09.055

Nagler, T., and Rott, H. (2000). Retrieval of wet snow by means of multitemporal SAR data. *IEEE Trans. Geoscience Remote Sens.* 38 (2), 754–765. doi: 10.1109/36.842004

Nearing, G. S., Moran, M. S., Scott, R. L., and Ponce-Campos, G. (2012). Coupling diffusion and maximum entropy models to estimate thermal inertia. *Remote Sens. Environ.* 119, 222–231. doi: 10.1016/J.RSE.2011.12.012

Pettinato, S., Santi, E., Brogioni, M., Paloscia, S., Palchetti, E., and Xiong, C. (2013). The potential of COSMO-SkyMed SAR images in monitoring snow cover characteristics. *IEEE Geoscience Remote Sens. Lett.* 10 (1), 9–13. doi: 10.1109/LGRS.2012.2189752

Pettinato, S., Bonvenga, F., Santi, E., Paloscia, S., Baroni, F., Belmonte, A., et al. (2022). "Monitoring of snow water equivalent and snowmelt through space-borne synthetic aperture radar techniques," in *52nd European Microwave Conference (EuMC)*, Milan, Italy, 91–94. doi: 10.23919/EuMC54642.2022.9924399

Picard, G., and Fily, M. (2006). Surface melting observations in Antarctica by microwave radiometers: correcting 26-year time series from changes in acquisition hours. *Remote Sens. Environ.* 104 (3), 325–336. doi: 10.1016/J.RSE.2006.05.010

Pogliotti, P., Guglielmin, M., Cremonese, E., di Cella, U., Filippa, G., Pellet, C., et al. (2015). Warming permafrost and active layer variability at cime bianche, Western european alps. *Cryosphere* 9 (2), 647–661. doi: 10.5194/tc-9-647-2015

Qin, Y., Abatzoglou, J. T., Siebert, S., Huning, L. S., AghaKouchak, A., Mankin, J. S., et al. (2020). Agricultural risks from changing snowmelt. *Nat. Clim. Change* 10 (5), 459–465. doi: 10.1038/s41558-020-0746-8

Quegan, S., and Yu, J. J. (2001). Filtering of multichannel SAR images. *IEEE Trans. Geoscience Remote Sens.* 39, 2373–2379. doi: 10.1109/36.964973

Ravasio, C., Garzonio, R., Di Mauro, B., Matta, E., Giardino, C., Pepe, M., et al. (2024). Retrieval of snow liquid water content from radiative transfer model, field data and PRISMA satellite data. *Remote Sens. Environ.* 311, 114268. doi: 10.1016/j.rse.2024.114268

Santi, E., De Gregorio, L., Pettinato, S., Cuozzo, G., Jacob, A., Notarnicola, C., et al. (2022). On the use of COSMO-SkyMed X-Band SAR for estimating snow water equivalent in alpine areas: a retrieval approach based on machine learning and snow models. *IEEE Trans. Geoscience Remote Sens.* 60, 1–19. doi: 10.1109/TGRS.2022.3191409

Semmens, K. A., Ramage, J., Bartsch, A., and Liston, G. E. (2013). Early snowmelt events: detection, distribution and significance in a major sub-arctic watershed. *Environ. Res. Lett.* 8 (1), 014020. doi: 10.1088/1748-9326/8/1/014020

Short, N. M., and Stuart, L. M. (1982). *The Heat Capacity Mapping Mission (HCMM) Anthology (NASA SP-465)*. Washington, DC: NASA Scientific and Technical Information Branch (in vendita tramite Superintendent of Documents, U.S. Government Printing Office).

Thirel, G., Salamon, P., Burek, P., and Kalas, M. (2013). Assimilation of MODIS snow cover area data in a distributed hydrological model using the particle filter. *Remote Sens.* 5 (11), 5825–5850. doi: 10.3390/rs5115825

Tian, J., Su, H., He, H., and Sun, X. (2015). An empirical method of estimating soil thermal inertia. *Adv. Meteorology* 2015, 428525–428529. doi: 10.1155/2015/428525

Van doninck, J., Peters, J., De Baets, B., De Clercq, E. M., Ducheyne, E., and Verhoest, N. E. C. (2011). The potential of multitemporal aqua and terra MODIS apparent thermal inertia as a soil moisture indicator. *Int. J. Appl. Earth Observ. Geoinform.* 13 (6), 934–941. doi: 10.1016/j.jag.2011.07.003

Wang, J., Bras, R. L., Sivandran, G., and Knox, R. G. (2010). A simple method for the estimation of thermal inertia. *Geophys. Res. Lett.* 37 (5), L05404. doi: 10.1029/2009GL041851

Wever, N., Jonas, T., Fierz, C., and Lehning, M. (2014). Model simulations of the modulating effect of the snow cover in a rain-on-snow event. *Hydrol. Earth Syst. Sci.* 18, 4657–4669. doi: 10.5194/hess-18-4657-2014

Xue, Y., and Cracknell, A. P. (1995). Advanced thermal inertia modelling. *Int. J. Remote Sens.* 16 (3), 431–446. doi: 10.1080/01431169508954411

Yue, X., Li, Z., Li, H., Wang, F., and Jin, S. (2022). Multi-temporal variations in surface albedo on Urumqi glacier No.1 in Tien Shan, under arid and semi-arid environment. *Remote Sens.* 14 (4), 808. doi: 10.3390/rs14040808